

Elastic crack propagation model for crystalline solids using a self-consistent coupled atomistic–continuum framework

Somnath Ghosh · Jiayi Zhang

Received: 30 January 2017 / Accepted: 1 July 2017
© Springer Science+Business Media B.V. 2017

Abstract Deformation and failure processes of crystalline materials are governed by complex phenomena at multiple scales. It is necessary to couple these scales for physics-based modeling of these phenomena, while overcoming limitations of modeling at individual scales. To address this issue, this paper develops self-consistent elastic constitutive and crack propagation relations of crystalline materials containing atomic scale cracks, from observations made in a concurrent multi-scale simulation system coupling atomistic and continuum domain models. The concurrent multi-scale model incorporates a finite temperature atomistic region containing the crack, a continuum region represented by a self-consistent crystal elasticity constitutive model, and a handshaking interphase region. Atomistic modeling is done by the molecular dynamics code LAMMPS, while continuum modeling is conducted by the finite element method. For single crystal nickel a nonlinear and nonlocal crystal elasticity constitutive relation is derived, consistent with the atomic potential function. An efficient, staggered solution scheme with parallel implementation is designed for the coupled problem. The atomistic–continuum coupling is

achieved by enforcing geometric compatibility and force equilibrium in the interphase region. Quantitative analyses of the crack propagation process focuses on size dependence, strain energy release rate, crack propagation rate and degradation of the local stiffness. The self-consistent constitutive and crack propagation relations, derived from the concurrent model simulation results are validated by comparing results from the concurrent and full FE models. Excellent accuracy and enhanced efficiency are observed in comparison with pure MD and concurrent model results.

Keywords Concurrent atomistic–continuum model · Crack propagation · Molecular dynamics · Finite element analysis · Self-consistent modeling · Multi-scale simulation

1 Introduction

Damage and failure of structural materials like metals and alloys involve deformation and failure mechanisms than span multiple length and time scales. These mechanisms can include bond-breaking or atomic separation at the atomic-scale, evolution of dislocation structures and other defects at the sub-micron scale, intra- and transgranular cracks in grains and grain boundaries at the micron-scale, and fracture zones in structural components at the macro-scale. While significant progress has been made in computational modeling of polycrystalline materials to predict deformation

S. Ghosh (✉)
M. G. Callas, Departments of Civil Mechanical and
Material Science Engineering, Johns Hopkins University,
3400 N. Charles St., Baltimore, MD 21218, USA
e-mail: sghosh20@jhu.edu

J. Zhang
Department of Civil Engineering, Johns Hopkins University,
3400 N. Charles St., Baltimore, MD 21218, USA

and stress–strain behavior with reasonable accuracy, failure predictions are still far from mature. A bottleneck for computational tools predicting failure is that the crack growth phenomena in complex crystalline microstructures are yet to be adequately understood and characterized. Very few models reliably predict the evolution of failure as observed in experiments. A popular way of modeling crack advance in polycrystalline systems is through the use of cohesive zone models (CZM) with parameters that are calibrated from experimental data. These models, e.g. in [Ortiz and Pandolfi \(1999\)](#), [Roe and Siegmund \(2003\)](#), define fracture as a gradual process, characterized by traction–separation relations in a process zone between crack surfaces. Various numerical models developed have been developed in this category. [Columbus and Grujicic \(2001\)](#), [Grujicic et al. \(2003\)](#) have combined CZM with crystal plasticity models to simulate crack propagation in crystalline solids. Their CZM traction–separation relations are determined from molecular statics simulations of the interface decohesion. While the CZM models are advantageous in terms of easy numerical implementation, in many cases they poorly represent deformation and other crack tip mechanisms governing crack growth. Considerable opportunities lie in developing physics-based crack evolution models that are informed by mechanisms and phenomena observed in atomistic simulations of crystalline solids. In this respect, robust, self-consistent framework coupling continuum scale deformation with atomic-scale crack evolution models to deduce continuum models of crack growth, could be valuable.

Current and previous research e.g. in [Shimomura et al. \(2003\)](#), [Farrissey et al. \(2000\)](#), [Zhu et al. \(2004\)](#), [Abraham et al. \(1997\)](#), [Zhou et al. \(1998\)](#), [Gumbusch \(1995\)](#), [Yamakov et al. \(2006\)](#), [Zhang and Ghosh \(2013\)](#) have shown that molecular dynamics or MD can be a powerful tool for studying the physical processes of crack growth related phenomena in the material microstructure. These studies have provided important insights on deformation mechanisms associated with crack initiation and propagation. A 320 billion atom simulation, using the two body Lennard-Jones (L-J) potential was conducted on the BlueGene/L in [Kadav et al. \(2006\)](#) to reach micron length scales. However, even with modern day high-performance computing resources, large-scale MD simulations of crack propagation in systems with continuum length and time scales is still a challenge. Extremely large degrees of

freedom in MD simulations tracking individual atoms in the ensemble put severe constraints on the extent of modeling both in spatial and temporal scales. This makes a case for developing continuum models of crack evolution conforming to observations made in atomistic simulations. Hierarchical upscaling is a convenient approach for simulating at the higher scales that involves extracting reduced order constitutive relations at the higher scale from lower scale MD simulations. Attempts of such upscaling to develop quantitative descriptions of crack growth from MD simulations has been made e.g. in [Spearot et al. \(2004\)](#), where a CZM is developed for interfacial crack in copper bi-crystals under normal and shear loading. Using results from MD simulations, traction–displacement relations for aluminum bi-crystal interfaces have been developed in [Yamakov et al. \(2006, 2008\)](#) and CZM parameters have been extracted for brittle cracks in [Zhou et al. \(2008\)](#). Since the reliability of these upscaled models is dependent on the accuracy of the lower scale model, insufficient MD domains with inappropriate boundary conditions can cost them inaccuracy.

Concurrent methods, which combine the lower scale MD and higher scale continuum descriptions into a single coupled description, are alternate approaches to multi-scale modeling. They let two systems evolve simultaneously, with traction reciprocity and compatibility conditions enforced at the interface. The models physically represent spatially larger systems and hence can help overcome the limitations of pure atomistic simulations. Various concurrent multi-scale models coupling atomistic and continuum systems have been developed, e.g. the quasi-continuum (QC) models ([Tadmor 1996](#); [Miller et al. 1998](#)), bridging domain models ([Xiao and Belytschko 2004](#)), atomistic-to-continuum models ([Badia et al. 2007, 2008](#)), embedded statistical coupling methods ([Saether et al. 2009](#)), coarse-grained atomistic models ([Xiong et al. 2012](#)) etc. While these methods have been effective in bridging the length-scale gap between simulations and experiments, unresolved issues still remain. The intrinsic differences in material descriptions and mechanisms with discrete and continuum models can give rise to significant errors at interfaces.

The goal of this paper is to develop physics-based self-consistent elastic constitutive and crack propagation relations for crystalline materials containing atomic scale cracks. These developments are from observations made in a concurrent multi-scale simula-

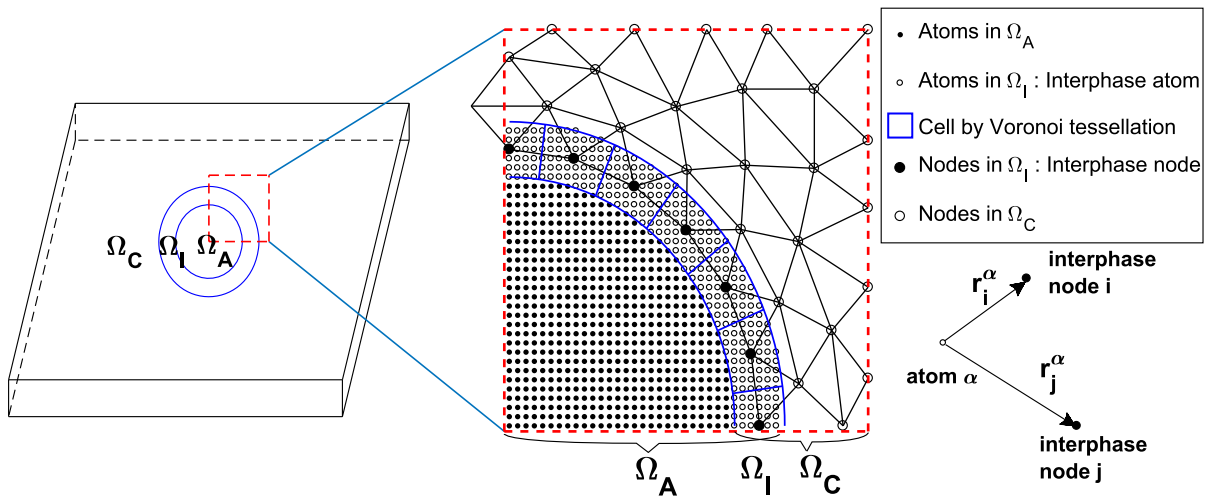


Fig. 1 Schematic of the partitioned computational domain, showing models for the MD, continuum and interphase regions

tion system coupling atomistic and continuum domain models. Only elastic continuum response of crystalline solids is considered in this paper. The concurrent multi-scale model incorporates a finite temperature atomistic region containing the crack, a continuum region represented by a self-consistent crystal elasticity constitutive model with degrading stiffness, and a handshake-interphase region. Atomistic simulations including a crack are conducted by the MD package LAMMPS (Plimpton 1995), while the continuum scale analysis are conducted by the finite element (FE) method. An efficient, staggered solution scheme with parallel implementation is designed for the coupled problem. The atomistic–continuum coupling is achieved by enforcing geometric compatibility and force equilibrium in the interphase region. In a multi-step approach, a finite temperature concurrent atomistic–continuum system that embeds a MD domain with a crack in an elastic continuum domain is first set up to develop a self-consistent continuum model for the field response near a crack. Next, the coupled concurrent model is used to simulate the crack growth process leading to the formulation of a continuum crack propagation relation for elastic media. This self-consistent constitutive-crack evolution model is then implemented in a continuum simulation for validation.

The paper starts with the formulation of the concurrent coupled atomistic–continuum model in Sect. 2. Numerical implementation of the coupled concurrent model is accomplished in Sect. 3. Section 4 discusses the self-consistent homogenized constitutive model for

a cracked solid, while crack propagation relations are developed in Sect. 5. The accuracy and efficiency of simulations with the self-consistent constitutive-crack evolution model are discussed in Sect. 6 and the paper concludes with a summary in Sect. 7.

2 A concurrent framework for coupled atomistic–continuum simulations

A concurrent simulation framework, coupling molecular dynamics (MD) and finite element (FE) continuum elasticity models for crystalline solids under quasi-static loading, is developed in this section. MD simulations are carried out by efficiently by the parallel Large-scale Atomic/Molecular Massively Parallel Simulator or LAMMPS (Plimpton 1995), while the FE simulations are conducted by codes developed in lead author’s group.

2.1 Embedding the atomistic domain in a continuum domain

As shown in Fig. 1, the computational domain is divided into three sub-domains for concurrent simulations. These include the atomistic domain Ω_A of MD simulations, the continuum domain Ω_C of finite element (FE) simulations and an “interphase” handshake domain Ω_I of compatibility constraints between MD and FE simulations. The FEM model for the continuum domain Ω_C assumes quasi-static conditions with inertia effects neglected. The constitutive model for Ω_C

is developed from self-consistent homogenization of results in the atomic portion of the model.

The interphase handshake region $\Omega_I = \Omega_A \cap \Omega_C$, where both the continuum and atomistic models overlap, is used to couple the sub-domains Ω_A and Ω_C . Following coupling methods discussed in Saether et al. (2009), Ω_I is comprised of a layer of finite elements with nodes characterized as “interphase nodes” and a band of underlying interphase atoms. Each interphase node in the FE model is associated with a cluster of interphase atoms, assigned using a 3D Voronoi tessellation method (Ghosh 2011). Compatibility conditions are enforced between each interphase node in the FE model and the cluster of interphase atoms. In this approach, spatially-averaged displacements of interphase atoms are equated to the displacement fields of the interphase node to implement the atom-node compatibility condition in a weak sense.

2.2 Governing equations

For solving a quasi-static continuum problem with linear kinematics and nonlinear material constitutive relations, an incremental formulation is developed. In the following development, indices α, β are used to denote finite element nodes, indices p, q identify atoms, and index i is used for coordinate axes. The equilibrium state for the quasi-static problem is obtained by minimizing the total potential energy functional. For a load increment from an equilibrated configuration in the small deformation framework, the incremented energy functional can be decomposed into contributions from the atomistic, continuum and interphase regions as:

$$\Delta\Pi_{tot} = \Delta\Pi_C + \Delta\Pi_A + \Delta\Pi_I \quad (1)$$

The first two terms in the RHS of Eq. (1) correspond to contributions from the continuum domain Ω_C and atomic domain Ω_A respectively, given as:

$$\begin{aligned} \Delta\Pi_C &= \int_{\Omega_C} \boldsymbol{\sigma} : \Delta\boldsymbol{\epsilon} dV - \int_{\partial\Omega_C} \mathbf{t} \cdot \Delta\mathbf{u}^C dA \\ &= \{\mathbf{f}_{C-int} - \mathbf{f}_{C-ext}\} \cdot \{\Delta\mathbf{u}^C\} \end{aligned} \quad (2a)$$

$$\Delta\Pi_A = \sum_{p \in \Omega_A} \Delta\Phi_p(\bar{\mathbf{r}}) - \sum_{p \in \Omega_A} \mathbf{f}_{A-ext}^p \cdot \Delta\bar{\mathbf{r}}_p \quad (2b)$$

For Eq. (2a), the first term on the RHS corresponds to the incremental strain energy in Ω_C , with $\boldsymbol{\sigma}$ and $\Delta\boldsymbol{\epsilon}$ rep-

resenting the Cauchy stress and incremental infinitesimal strain tensors respectively. The second term corresponds to the work potential due to the applied traction vector \mathbf{t} on the boundary of the domain $\partial\Omega_C$. Note that the kinetic energy contribution to the overall energy is neglected for quasi-static systems. The internal force vector $\{\mathbf{f}_{C-int}\} = \bigcup_{\alpha \in \Omega_C} \{\mathbf{f}_{C-int}^\alpha\}$ is the equivalent internal force from the strain energy, and is given as the union of force vectors at every node α of the FE mesh in $\partial\Omega_C$. It is evaluated from the derivative of the discretized form of the total strain energy of the FE domain with respect to nodal degrees of freedom $\Delta\mathbf{u}^C$. On the other hand, the external force vector $\{\mathbf{f}_{C-ext}\}$ on all boundary nodes of the FE mesh is computed from the applied traction on the FE boundary $\partial\Omega_C$.

For the atomistic Eq. (2b), $\Delta\Phi_p(\bar{\mathbf{r}})$ is the incremental energy of an atom p given in terms of the interatomic potential as function of position vector of all atoms $\bar{\mathbf{r}}$. The multi-body potential function described by the embedded-atom method (EAM) (Mishin et al. 1999) is used in this analysis for metallic systems. The term \mathbf{f}_{A-ext}^p denotes external forces applied on an atom p from external sources and $\Delta\bar{\mathbf{r}}_p$ is the position vector increment of the atom p . The summation is over all atoms in Ω_A . Since inertia is neglected for the continuum FE analysis, the atomic motion due to thermal fluctuation is time-averaged for coupling the response of the temporally disparate domains. The relation between the displacement vector \mathbf{r}_p of atom p and its time-averaged value $\bar{\mathbf{r}}_p$ is expressed as:

$$\bar{\mathbf{r}}_p(t) = \frac{1}{N} \sum_{j=0}^{N-1} \mathbf{r}_p(t - j \cdot \Delta t^{md}) \quad (3)$$

where $\mathbf{r}_p(t)$ is the position vector of an atom p at time t and Δt^{md} is the uniform time step taken in the N time-integration steps for MD simulations. $N \Delta t^{md}$ should be chosen larger than the period T of thermal vibration of the atomistic system such that the average does reflect the displacement due to mechanical loading. In this paper, T is set to be 1 ps with $N = 500$ and $\Delta t^{md} = 2 fs$.

The contribution to the energy in Eq. (1) from the handshake domain Ω_I is obtained from the constraint compatibility condition. Using Lagrange multipliers, this constraint condition can be implemented as:

$$\Delta\Pi_I = \sum_{\beta \in \Omega_I} \lambda_\beta \cdot \mathbf{C}_\beta \quad (4)$$

where $\lambda_\beta = \{\lambda_\beta^1, \lambda_\beta^2, \lambda_\beta^3\}$ is an array of Lagrange multipliers for the constraint function $C_\beta = \{C_\beta^1, C_\beta^2, C_\beta^3\}$ at an interphase node β . The constraint function C_β describes the geometry compatibility of a interphase node β in Ω_I , where the average displacement of atoms inside the Voronoi cell G_β (see Fig. 1) equals to the displacement of that node. For an incremental displacement field, the relation is given as:

$$C_\beta(\Delta u^C, \Delta u^A) = \Delta u_\beta^C - \sum_{p \in G_\beta} w_p \cdot \Delta u_p^A = 0 \quad \forall \beta \in \Omega_I \tag{5}$$

where $u_p = r_p - r_p^0$ is the displacement vector of atom p and u_β is the displacement vector of interphase node β . The summation contains a weighting function w_p for atom $p \in G_\beta$ with $\sum_{p \in G_\beta} w_p = 1$. The superscripts C and A will be dropped in the subsequent discussions as their association with the node number β or the atom number p automatically designate their domain. For coupling finite temperature atomistic simulations with quasi-static continuum simulations, a time-averaged displacement vector \bar{u}_p , corresponding to the atomic position vector defined in Eq. (3), is used. The corresponding compatibility condition is expressed as:

$$\begin{aligned} \Delta u_\beta(t) &= \sum_{p \in G_\beta} w_p \cdot \Delta \bar{u}_p(t) \\ &= \sum_{p \in G_\beta} w_p \cdot \frac{1}{N} \left[\sum_{j=0}^{N-1} \Delta u_p(t - j \cdot \Delta t^{md}) \right] \end{aligned} \tag{6}$$

The equilibrium condition of the coupled system is obtained by setting the first variation of the energy functional (1) to zero, i.e. $\delta(\Delta \Pi_{tot}) = 0$. Substituting Eqs. (2a), (2b), (4) and (5) into Eq. (1), this condition is derived for nodal points in the continuum FE domain and atoms in the MD domain for directions $i = 1, 2, 3$ as:

$$\begin{aligned} \frac{\partial \Delta \Pi_{tot}}{\partial \Delta u_\alpha^i} &= f_\alpha^i \\ &= \begin{cases} (f_\alpha^i)_{int} - (f_\alpha^i)_{ext} + \lambda_\alpha^i & \text{for node } \alpha \in \Omega_I \\ (f_\alpha^i)_{int} - (f_\alpha^i)_{ext} & \text{for node } \alpha \in \Omega_C \setminus \Omega_I \end{cases} \\ &= 0 \end{aligned} \tag{7a}$$

$$\frac{\partial \Delta \Pi_{tot}}{\partial \Delta \bar{r}_p^i} = f_p^i$$

$$\begin{aligned} &= \begin{cases} \frac{\partial \Delta \Phi(r)}{\partial \Delta \bar{u}_p^i} - (f_p^i)_{ext} - w_p \lambda_\alpha^i & \text{for atom } p \in G_\alpha \text{ in } \Omega_I \\ \frac{\partial \Delta \Phi(r)}{\partial \Delta \bar{u}_p^i} - (f_p^i)_{ext} & \text{for atom } p \in \Omega_A \setminus \Omega_I \end{cases} \\ &= 0 \end{aligned} \tag{7b}$$

where G_α is the Voronoi cell domain associated with finite element node α . In Eq. (7a) the total conjugate force component f_α^i at a node α is from contributions due to strain energy $(f_\alpha^i)_{int}$, external forces $(f_\alpha^i)_{ext}$ and Lagrange multipliers λ_α^i representing reaction force on node α from atomistic system due to compatibility constraint. For the atomistic domain, f_p^i is the time-averaged total conjugate force component on an atom p in its time-averaged position \bar{r}_p^i . The constraint force contribution to individual atoms is $w_p \lambda_\alpha^i$, where w_p is a weighting function, such that:

$$(\lambda_\alpha^i)^C + \left(\sum_{p \in G_\beta} w_p \lambda_\alpha^i \right)^A = 0 \tag{8}$$

The MD equations in the domain Ω_A , needed for solving the coupled Eq. (7) yielding thermal fluctuations of atoms, are given by:

$$m_p \ddot{u}_p = f_p \tag{9}$$

where m_p is the mass of an atom p with an applied force f_p . To maintain the temperature of the system and absorb elastic waves, temperature control is applied through Langevin dynamics on the atoms in the interphase region Ω_I . The NVE ensemble is used for the pure atomistic domain Ω_A , with additional random force plus damping applied. Thus the forces on the interior atoms remain unchanged, while the forces on interface atoms are given as:

$$f_p = f_p^0 - \gamma m_p \dot{r}_p + \sqrt{2\gamma k_B \theta m_p} R(t) \quad \forall p \in \Omega_I \tag{10}$$

where m_p is the mass, $f_p^0 = -\nabla_p \Phi + w_p \lambda_\beta + f_{A-ext}^p$ is the initial force as given by Eq. (7b), k_B is the Boltzmann constant, θ is the target temperature, γ is the damping coefficient, and $R(t)$ is a delta-correlated stationary Gaussian process with zero-mean value. The damping term in Eq. (10) helps suppress the elastic wave propagation in the interface region. This is important for numerical stability of the dynamic coupled model.

3 Numerical implementation of the coupled concurrent model

The governing Eq. (7) of the coupled atomistic–continuum system are solved incrementally for quasi-static equilibrium under varying loading conditions, using a successive iterative approach with interphase load-balancing. Specifically, a staggered-iterative solution approach is followed. This approach solves respective problems for the domains Ω_C and Ω_A separately in each iteration subject to the displacement and constraint forces condition passed through the interphase domain Ω_I . It enables the utilization of appropriate algorithms and solvers for each domain. Ghost forces are mitigated by using a dead load correction method proposed in Shenoy et al. (1999). Appropriate interphase modules and data structure are used in the integration of both the MD and FE codes. In addition, a driver code is written for information passing between the FE and MD modules by using MPI libraries.

3.1 Setting up the relaxed initial configuration in Ω_A

The equilibrium configuration of the atomic region is established prior to the start of simulation of the coupled model. The atomistic model is initially created for the entire domain i.e. $\Omega_T = \Omega_C \cup \Omega_A$ conforming to the crystallographic lattice configuration. Subsequently, an energy minimization process under zero-temperature molecular statics conditions is used to obtain the initial equilibrium configuration. After that, the atoms in the continuum domain $\Omega_C \setminus \Omega_I$ are removed and the finite element mesh is created in Ω_C . In interphase region Ω_I , where both atoms and finite element mesh co-exist, the atoms–nodes connection is built by Voronoi tessellation. To model cracks in the atomistic domain, the interaction between atoms on two sides of crack are turned off.

3.2 Sequence of steps in a time step

In a time increment from t to $t + \Delta t$ in the quasi-static analysis, let ΔU^C and $\Delta \bar{U}^A$ be the converged incremental displacement solutions of the FE nodes in Ω_C and time-averaged atomic motion in Ω_A respectively, i.e.

$$U^C(t + \Delta t) = U^C(t) + \Delta U^C(t) \in \Omega_C \quad \text{and}$$

$$\bar{U}^A(t + \Delta t) = \bar{U}^A(t) + \Delta \bar{U}^A(t) \in \Omega_A \quad (11)$$

The displacement increment $\Delta U^C(t)$ can be further partitioned into a group of displacement increments $\Delta U^{C_I}(t)$ of the interphase nodes in $\Omega_{C_I} (\in \Omega_I) = \Omega_C \cap \Omega_A$ and displacement increments $\Delta U^{C_O}(t)$ of all other nodes in $\Omega_{C_O} = \Omega_C \setminus \Omega_I$, i.e.

$$\Delta U^C(t) = \begin{Bmatrix} \Delta U^{C_I}(t) \\ \Delta U^{C_O}(t) \end{Bmatrix} \quad (12)$$

An incremented external load is typically applied on the external boundary $\partial \Omega_{C_O}$ of the coupled system. The corresponding discretized equilibrium equations for the continuum system at time $t + \Delta t$ is expressed using Eq. (7a) as:

$$\begin{Bmatrix} f_{\text{int}}^{C_I}(t + \Delta t) \\ f_{\text{int}}^{C_O}(t + \Delta t) \end{Bmatrix} - \begin{Bmatrix} f_{\text{ext}}^{C_I}(t + \Delta t) \\ f_{\text{ext}}^{C_O}(t + \Delta t) \end{Bmatrix} + \begin{Bmatrix} \lambda(t + \Delta t) \\ 0 \end{Bmatrix} = 0 \quad (13)$$

where $f_{\text{int}}^{C_I}$ and $f_{\text{int}}^{C_O}$ are the internal nodal force vectors from the strain energy contributions in Ω_{C_O} and Ω_{C_I} , $f_{\text{ext}}^{C_I}$ and $f_{\text{ext}}^{C_O}$ are externally applied load vectors on $\partial \Omega_{C_O}$ and $\partial \Omega_{C_I}$, and λ corresponds to the vector of Lagrange multipliers that are associated with displacement constraints in the continuum–atomistic hand-shake region, all at the end of the time-step at $(t + \Delta t)$. In an incremental formulation, the vectors are additively decomposed as:

$$\begin{aligned} \{f_{\text{int}}^C(t + \Delta t)\} &= \{f_{\text{int}}^C(t)\} + \{\Delta f_{\text{int}}^C\} \\ \{f_{\text{ext}}^C(t + \Delta t)\} &= \{f_{\text{ext}}^C(t)\} + \{\Delta f_{\text{ext}}^C\} \\ \{\lambda(t + \Delta t)\} &= \{\lambda(t)\} + \{\Delta \lambda\} \end{aligned} \quad (14)$$

In every successive iteration step k of the staggered scheme, the internal nodal forces $\{\Delta f_{\text{int}}^C\}$ can be expressed in terms of the infinitesimal displacement vector $\{\Delta U^C\}$, by neglecting higher order terms, as:

$$\{\Delta f_{\text{int}}^C\}^k = \left\{ \frac{\partial \Delta f_{\text{int}}^C}{\partial \Delta U^C} \right\}^k \cdot \{\Delta U^C\}^k = [K^C]^k \{\Delta U^C\}^k \quad (15)$$

where $[K^C]^k$ is the secant stiffness matrix in the $k - th$ iteration given as:

$$[\mathbf{K}^C]^k = \begin{bmatrix} \mathbf{K}^{C-II} & \mathbf{K}^{C-IO} \\ \mathbf{K}^{C-OI} & \mathbf{K}^{C-OO} \end{bmatrix}^k = \begin{bmatrix} \frac{f_{int}^{C_I}}{\Delta U^{C_I}} & \frac{f_{int}^{C_I}}{\Delta U^{C_O}} \\ \frac{f_{int}^{C_O}}{\Delta U^{C_I}} & \frac{f_{int}^{C_O}}{\Delta U^{C_O}} \end{bmatrix}^k \quad (16)$$

With equilibrium condition satisfied at time t , and the assumption that no external load is applied on the interphase boundary $\partial\Omega_{C_I}$, the Eq. (13) can be rewritten for the k -th iteration step as:

$$\begin{bmatrix} \mathbf{K}^{C-II} & \mathbf{K}^{C-IO} \\ \mathbf{K}^{C-OI} & \mathbf{K}^{C-OO} \end{bmatrix}^k \begin{Bmatrix} \Delta U^{C_I} \\ \Delta U^{C_O} \end{Bmatrix} - \begin{Bmatrix} 0 \\ \Delta f_{ext}^{C_O} \end{Bmatrix} + \begin{Bmatrix} \Delta \lambda \\ 0 \end{Bmatrix}^k = 0 \quad (17)$$

In the time increment from t to $t + \Delta t$, with displacement fields $\Delta U^C(t)$ and $\Delta \bar{U}^A(t)$ known for iteration step $k \geq 1$, the search for solution fields in the $k + 1 - th$ iteration step proceeds along the following steps.

I. Displacement increments in Ω_C : This steps solves the finite element Eq. (17) for the continuum domain Ω_C with known boundary conditions on the external boundary $\partial\Omega_C^{ext}$, as well as displacements on the interphase nodes in the handshake region Ω_I . The incremental load (or displacement) on $\partial\Omega_C^{ext}$ is held fixed for the time increment Δt . At an interphase node β , the time-averaged displacement vector ΔU^{A_I} is given as:

$$\{\Delta U_{\beta}^{A_I}\}^k = \sum_{p \in G_{\beta}} w_p \cdot \Delta \{\bar{U}_p^A\}^k \quad (18)$$

In every iteration step, updated nodal displacements are applied in the handshake domain Ω_{C_I} , corresponding to atomistic displacements in Ω_{A_I} in the previous iteration, as:

$$\{\Delta U^{C_I}\}^{k+1} = \{\Delta U^{A_I}\}^k \quad (19)$$

Subsequently, the Eq. (17) is solved for the displacements $\{\Delta U^{C_O}\}^{k+1}$ and Lagrange multipliers $\{\Delta \lambda\}^{k+1}$ using a nonlinear solver like the Newton–Raphson method or the quasi-Newton method.

II. Constraint forces on Ω_{A_I} from Ω_{C_I} With the known vector of Lagrangian multipliers $\{\lambda\}^{k+1} = \{\lambda\}^k + \{\Delta \lambda\}^{k+1}$ for all interphase nodes, constraint forces on atoms in Ω_{A_I} are evaluated using Eq. (8) as:

$$\{f_p^{constraint}\}^{k+1} = \begin{cases} w_p \{\lambda_{\beta}\}^{k+1} & \forall p \in G_{\beta} \in \Omega_{A_I} \\ 0 & \forall p \in \Omega_A \setminus \Omega_{A_I} \end{cases} \quad (20)$$

III. MD simulations of domain Ω_A with constraint forces The constraint forces in step II are applied to the atomistic domain Ω_A for MD simulations over a time period of the $T_A = N \Delta t^{md}$ using the velocity Verlet time algorithm (Plimpton 1995) for integrating Eq. (9). The time-averaged displacement vector $\{\bar{u}_p\}^{k+1}$ is evaluated using Eq. (3).

$$\{\bar{u}_p\}^{k+1} = \frac{1}{N} \sum_{j=0}^{N-1} \mathbf{u}_p(t - j \cdot \Delta t^{md}) \quad \forall p \in \Omega_A \quad (21)$$

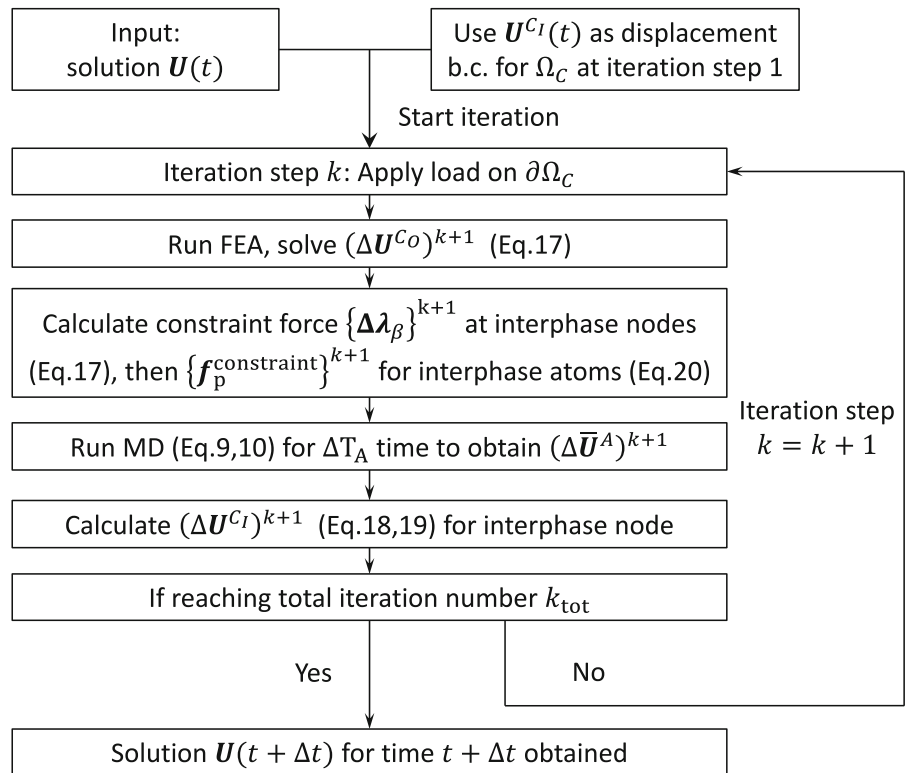
IV. Transfer displacements from Ω_{A_I} to Ω_C With the atomic displacements obtained from Eq. (21), $\Delta U_{k+1}^{A_I}$ is calculated using Eq. (18). This serves as the displacement boundary condition for the finite element interphase nodes in the next iteration.

The staggered, successive iterative solution procedure, with a fixed applied load in each increment can lead to large deviation from the equilibrium configuration in the initial iteration cycles. A sub-stepping algorithm is implemented to reduce the stress fluctuation in the the staggered process. The load increment is uniformly distributed over a pre-assessed number of sub-steps in the increment. Each continuum-atomistic iteration is conducted over a sub-step $\Delta_k T_A$ of the total time increment $\Delta t = \sum_k^{k_{tot}} \Delta_k T_A$. $\Delta_k T_A$ incorporates N times steps in the MD simulations, i.e. $N = \frac{\Delta_k T_A}{\Delta t^{md}}$. The choice of the number of iterations k_{tot} is governed by the characteristic time t_c that is derived from the size of atomic domain divided by the velocity of sound in the material. For the specimen used in this paper, this is derived to be $t_c \approx 10$ ps. To ensure that the effect of the applied loading has traveled through the MD domain for the system to equilibrate, numerical tests are conducted and a time $4t_c$ is found to be sufficient. In this work, k_{tot} is taken as 40 and $\Delta_k T_A$ is taken as 1 ps. This corresponds to $\Delta t = 40$ ps. A flow chart of the update process in a time step Δt is given in Fig. 2.

4 Self-consistent homogenized constitutive model of cracked solid

The self-consistent method estimates the overall material response by embedding a heterogeneous domain in a large homogeneous material with yet unknown macroscopic properties (Budiansky 1965; Hill 1965). Self-consistent homogenization determines the constitutive relations, while maintaining equilibrium of

Fig. 2 Flow chart of the staggered solution process for the concurrently coupled model under finite temperature conditions



disparate domains under the kinematic compatibility constraint. In this section, a self-consistent constitutive model is derived for an elastic crystalline material containing a crack using the coupled concurrent computational model. Self-consistency of the governing equations, requires the stress–strain relations in the continuum media to be consistent with the inter-atomic potential of the discrete atomic domain that exclusively contains the crack. The model is further used to investigate the crack propagation that is quantified in terms of the rate of energy and kinematic variables. Though the results of crack propagation are calibrated for a specified orientation in a single crystal nickel with the EAM potential (Mishin et al. 1999), the approach here is general and can be applied to a variety of materials.

The constitutive model developed in consistency with the behavior of the atomic domain is assumed to be elastic in this paper. An assumption made for the self-consistent elastic model is that different features (e.g. dislocations) belonging to a domain remain confined and do not cross-over from one domain to the other. Nonlinearity is expected in the material constitutive relation even in the elastic range, due to the non-harmonic EAM potential of atomic interaction.

Furthermore, nonlocal constitutive relations are generally associated with size-effects and length scales, that may be related to the material microstructure, defects structure, cracks or features like atomic interaction. In defining the nonlinear, nonlocal elasticity relations, the Cauchy stress is additively decomposed into two parts as:

$$\sigma_{ij} = \sigma_{ij}^{loc} + \hat{\sigma}_{ij} \quad (22)$$

where σ_{ij}^{loc} is the local stress term that is a nonlinear function of the strain, and $\hat{\sigma}_{ij}$ is the nonlocal term that is associated with the strain gradient.

4.1 Calibrating nonlinear terms

For obtaining the nonlinear effect on local term σ_{ij}^{loc} , a third-order expansion of the strain energy density function in terms of the strains is expressed as:

$$\omega(\epsilon) = \frac{1}{2!} c_{ijkl} \epsilon_{ij} \epsilon_{kl} + \frac{1}{3!} c_{ijklmn} \epsilon_{ij} \epsilon_{kl} \epsilon_{mn} \quad (23)$$

here c_{ijkl} and c_{ijklmn} correspond to the first and second order stiffness coefficients respectively. For cubic pure nickel single crystals, the coefficients are subjected to

Table 1 Calibrated values of first and second order stiffness coefficients (unit:GPa) and comparison with results in [Sarma and Reddy \(1973\)](#), [Mishin et al. \(1999\)](#)

Source	c_{11}	c_{12}	c_{44}	c_{111}	c_{112}	c_{123}	c_{144}	c_{166}	c_{456}
Calibrated	244.6	150.8	125.1	-1660	-1220	-250	-130	-510	-65
Ref. Sarma and Reddy (1973)	251.6	154.4	122.0	-2032	-1043	-220	-138	-910	-70
Ref. Mishin et al. (1999)	247	148	125						

crystal symmetry group constraints. Using contracted notations in the representation of the tensors i.e.

$$11 \mapsto 1, 22 \mapsto 2, 33 \mapsto 3, 23 \mapsto 4, 31 \mapsto 5, 12 \mapsto 6$$

the coefficients in Eq. (23) are reduced to only 3 independent coefficients c_{11} , c_{12} and c_{44} for the first-order stiffness and 6 independent coefficients c_{111} , c_{112} , c_{123} , c_{144} , c_{166} and c_{456} for the second order stiffness. With this reduction, Eq. (23) becomes:

$$\begin{aligned} \omega(\epsilon) = & \frac{1}{2}c_{11}(\epsilon_1^2 + \epsilon_2^2 + \epsilon_3^2) + c_{12}(\epsilon_1\epsilon_2 + \epsilon_2\epsilon_3 + \epsilon_3\epsilon_1) \\ & + \frac{1}{2}c_{44}(\epsilon_4^2 + \epsilon_5^2 + \epsilon_6^2) + \frac{1}{6}c_{111}(\epsilon_1^3 + \epsilon_2^3 + \epsilon_3^3) \\ & + \frac{1}{2}c_{112}(\epsilon_1^2(\epsilon_2 + \epsilon_3) + \epsilon_2^2(\epsilon_3 + \epsilon_1) + \epsilon_3^2(\epsilon_1 + \epsilon_2)) \\ & + c_{123}\epsilon_1\epsilon_2\epsilon_3 + \frac{1}{2}c_{144}(\epsilon_1\epsilon_4^2 + \epsilon_2\epsilon_5^2 + \epsilon_3\epsilon_6^2) \\ & + \frac{1}{2}c_{166}(\epsilon_1(\epsilon_5^2 + \epsilon_6^2) + \epsilon_2(\epsilon_6^2 + \epsilon_4^2) + \epsilon_3(\epsilon_4^2 + \epsilon_5^2)) \\ & + c_{456}\epsilon_4\epsilon_5\epsilon_6 \end{aligned} \quad (24)$$

The first three terms corresponds to the harmonic part of the EAM potential and the remaining to the non-harmonic part.

Biaxial tension simulations of an uncracked specimen are conducted by the coupled concurrent model to calibrate the 9 stiffness coefficients in Eq. (24). The calibration is based on the minimization of the L_2 norm $\|\mathbf{F}^{A_I} - \mathbf{F}^{C_I}\|$ in interphase region. Calibrated values of the stiffness coefficients are given in Table 1 and compared with values from experiments and ab-initio calculations in [Sarma and Reddy \(1973\)](#), [Mishin et al. \(1999\)](#). The calibrated parameters from the coupled concurrent model simulations generally agree with the values given in the references.

4.2 Calibrating nonlocal terms

The non-local effect is accounted for through the incorporation of gradient elasticity terms in the constitutive relations. Studies in [Askes and Aifantis \(2011\)](#),

[Maranganti and Sharma \(2007\)](#), [Aifantis \(1984\)](#) suggest that the first gradient is commonly neglected in the nonlocal stress representation. The gradient elasticity formulation expresses the nonlocal term $\hat{\sigma}_{ij}$ in Eq. (22) in terms of a single length-scale parameter l as:

$$\hat{\sigma}_{ij} = l^2 c_{ijmn} \nabla^2 \epsilon_{mn} \quad (25)$$

where c_{ijmn} are the first order stiffness coefficients given in Eq. (23). The nonlocal term is the combined effect of an intrinsic material length-scale l and the local strain gradient that is dependent on topology and loading conditions. Assuming that the K-field governs the strain in the vicinity of the crack, i.e.

$$\epsilon_{ij}(r, \theta) = \frac{A_{ij}}{\sqrt{r}} B_{ij}(\theta) \quad (26)$$

where r is distance from the tip and A_{ij} are constants proportional to the stress intensity factor K_I , Eq. (25) yields:

$$\nabla^2 \epsilon_{ij} \propto \frac{1}{r^2} \epsilon_{ij} \quad (27)$$

Correspondingly the ratio $\frac{\hat{\sigma}_{ij}}{\sigma_{ij}^{\text{loc}}} \sim \mathcal{O}(\frac{l^2}{r^2})$. Thus if the distance of continuum elements from crack tip is $r \gg l$, nonlocal elasticity may be ignored.

Calibration of the length scale parameter is done by conducting molecular statics simulation of a single crystal nickel specimen with a center crack as shown in Fig. 3a that is introduced to create a strain-gradient field. The specimen dimensions are $L_x = L_y = 50$ nm, $L_z = 4.224$ nm, and the crack is of length is $2a_0 = 20$ nm in the xz-plane through z direction. A biaxial displacement loading is applied in the x and y directions on the lateral boundaries, while periodic boundary condition with stress free conditions are applied on the z-faces. To evaluate the nonlocal stresses $\hat{\sigma}_{ij}$, the virial stress field σ_{ij} and the local stress field σ_{ij}^{loc} are calculated using Eq. (24) and parameters in

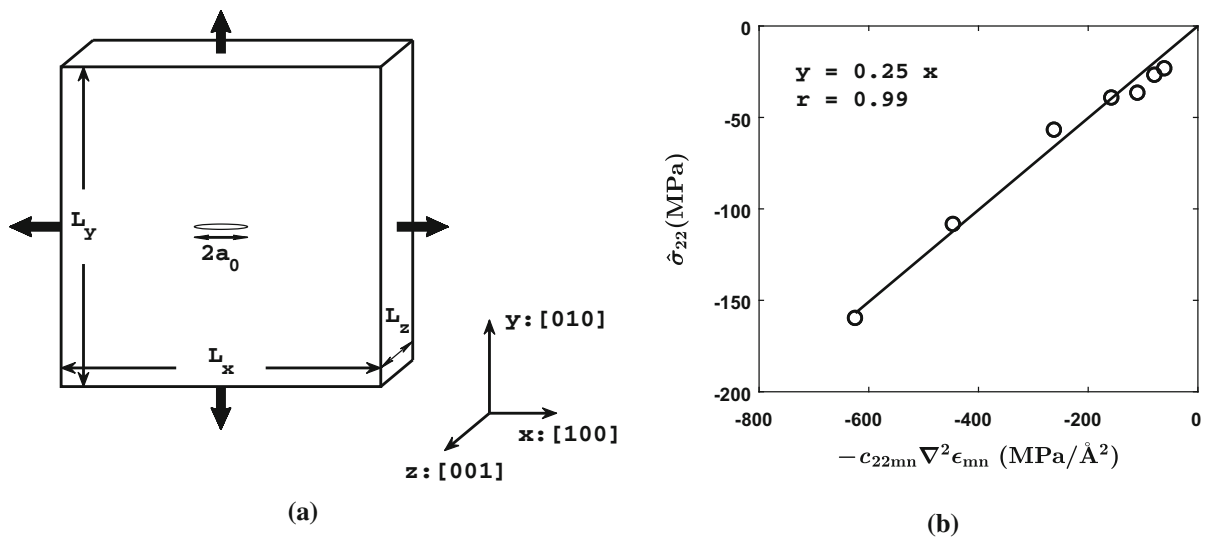


Fig. 3 **a** Nickel specimen with EAM potential for molecular statics simulation on sample with an embedded center crack, and **b** plot of the nonlocal stress as a function of strain gradient. The slope corresponds to the square of l^2

Table 1, which is followed by evaluating the local deformation gradient and strain fields using a least-square minimization-based methodology for atomic lattices proposed in Zimmerman et al. (2009) and implemented in Zhang and Ghosh (2013). Figure 3b plots the stress $\hat{\sigma}_{22} = \sigma_{ij} - \sigma_{ij}^{\text{loc}}$ as a function of $[-c_{22mn} \nabla^2 \epsilon_{mn}]$ for atoms in the x -direction in front of crack tip. The calibrated length scale parameter l^2 for nickel using the EAM potential, corresponding to the slope of this plot is $l \approx 0.5 \text{ \AA}$. This is consistent with values for f.c.c metals copper and aluminum given in Maranganti and Sharma (2007).

4.3 Validating the self-consistent constitutive model

To validate the developed nonlinear and nonlocal constitutive model, the crack tip stress field calculated by full atomistic simulations with molecular statics is compared with the stress field of the same domain but by continuum simulations with a finite element model. Two different constitutive relations are used for the finite element model. One is a linear elastic constitutive relation, while the other is the self-consistent constitutive relation developed in Sect. 4. The specimen domain is the same as that shown in Fig. 3a. It is subjected to biaxial loading in the x and y directions and is stress free in the z direction.

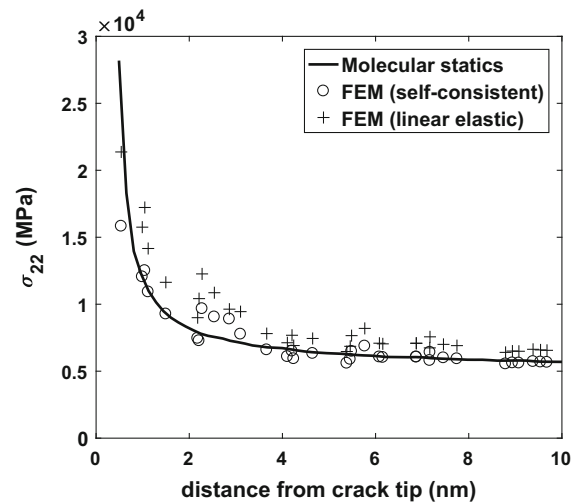


Fig. 4 Comparison of stress component σ_{22} near the crack tip generated by atomistic simulations using molecular statics, and finite element simulations using linear elastic and self-consistent constitutive models respectively

Figure 4 shows that the linear elastic constitutive relation overestimates the stress, while the self-consistent constitutive law has good consistency with the full atomistic model. The results indicate that the crack-tip stress field is more accurately represented by the self-consistent constitutive model developed in this study.

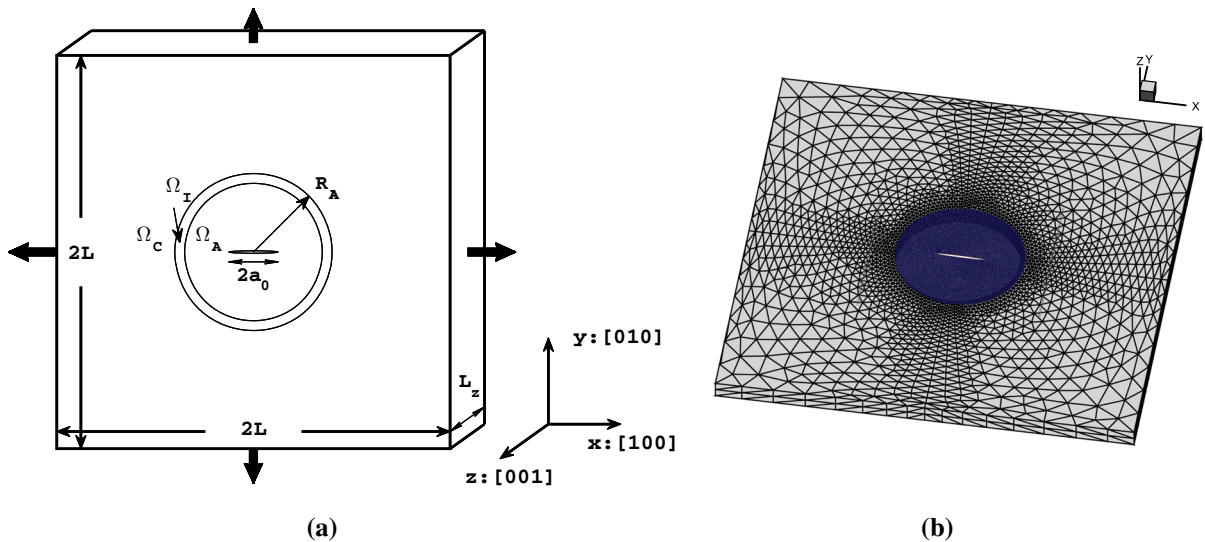


Fig. 5 **a** Geometry of the specimen with loading, and **b** the FE continuum domain and atomistic domain used in the concurrent atomistic–continuum model for crack propagation

5 Developing crack propagation relations from the atomistic–continuum framework

The concurrent atomistic–continuum model along with the self-consistent constitutive framework is implemented to investigate characteristics of crack propagation in single crystal nickel. A parametric crack propagation law is derived from the resulting simulation data, addressing both kinematic and thermodynamic aspects in the continuum description. Length-scale dependence is explored in the crack propagation process and results of the concurrent model are compared to that from a full MD model.

5.1 Setting up the concurrent model for the crack propagation simulations

The geometry and loading conditions for simulation specimen in the concurrent atomistic–continuum model is shown in Fig. 5a. The dimensions of the specimen computational domain are $200 \text{ nm} \times 200 \text{ nm} \times 4.224 \text{ nm}$ in the coordinate system shown. The atomistic domain Ω_A is a cylinder of radius $R_A = 32 \text{ nm}$, containing about 1.3 million atoms. The interphase region Ω_I is an annular ring region with inner and outer radius 28 nm and 32 nm respectively. The lattice structure of nickel is face centered cubic or fcc with lattice constant 3.52 \AA and lattice orientation is given as

$x \rightarrow [100]$, $y \rightarrow [010]$ and $z \rightarrow [001]$. A pre-existing center crack is created in the xz -plane with length $2a_0 = 20 \text{ nm}$ by removing a row of atoms through the entire specimen thickness in the z -direction as shown in Fig. 5a. The continuum domain part of the domain Ω_C is discretized into a finite element mesh containing approximately 20,000 4-noded constant strain tetrahedral elements and approximately 5000 nodes as shown in Fig. 5b.

After initial relaxation of the MD model as discussed in Sect. 3.1, a bi-axial displacement loading is applied in the x and y directions at a constant strain-rate up to a total strain of $\epsilon_{11} = \epsilon_{22} = 3.5\%$. Periodic boundary with stress free conditions $\sigma_{33} = 0$ are applied on the z -faces. The continuum domain uses the nonlinear-nonlocal elasticity relations in Eq. (22) developed in Sect. 4. The NVE ensemble is used for MD simulation and the temperature of atomistic domain is set to 1 K by applying the Langevin thermostat in the interphase region. The strain-rate applied is $5 \times 10^7 \text{ s}^{-1}$ with time-step $\Delta t^{md} = 2 \text{ fs}$. Each sub-step $\Delta_k T_A$ in the continuum-atomistic iteration in Sect. 2.2 incorporates $N = 500$ times steps and hence $\Delta_k T_A = 1 \text{ ps}$. To investigate the accuracy of the coupled concurrent model as well as the effect of the boundary condition on crack propagation, three different sizes, viz. $L = 50$, 100 and 200 nm are considered. The specimen sizes $L = 100$ and 200 nm are modeled by the concurrent model, while

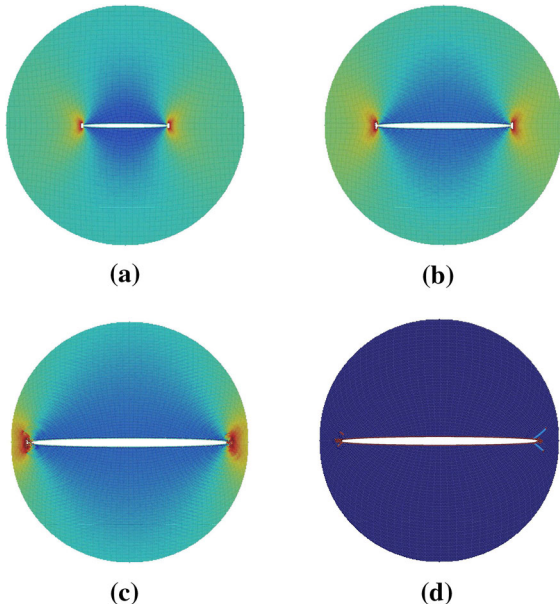


Fig. 6 **a, b, c** Contour plots of the virial stress σ_{22} at overall strains $\epsilon_{22} = 3.0, 3.35$ and 3.39% respectively, and **d** contour plot of common neighbor analysis (CNA) map at an overall strain $\epsilon_{22} = 3.39\%$ in the atomistic domain of the concurrent model, showing crack propagation and dislocation emission

specimen sizes $L = 50$ and 100 nm are modeled by pure MD. A direct comparison of results by the two models is made for the size $L = 100$ nm.

5.2 Simulation results

The concurrent atomistic–continuum simulations indicate that the crack starts to propagate symmetrically in the x direction by bond cleavage at strain levels of $\epsilon_{11} = \epsilon_{22} \approx 3.2\%$, $\sigma_{33} = 0$. The propagation occurs on the original crack surface in a symmetric manner about the y -axis. Dislocation emission is observed from the crack tips after the crack propagates about 10 nm propagation on each side. Contour plots of the local virial stress with snapshots of sequential crack propagation are shown in Fig. 6. Figure 6a, b, c show the contours of the local virial stress component σ_{22} with increasing cleavage crack at overall strain levels $\epsilon_{22} = 3.0, 3.35$, and 3.39% respectively. Figure 6d shows the contour of the local common neighbor analysis (CNA) map at an overall strain $\epsilon_{22} = 3.39\%$. CNA (Honeycutt and Anderson 1987; Zhang and Ghosh 2013), which is based on a nearest-neighbor map, is sensitive to the deformation of atoms in the ensemble

and can accurately identify the defect structure. Figure 6d shows dislocation emission at the crack tips following initial brittle crack propagation. vaFor quantitative insights on the brittle crack propagation process, three aspects are studied viz. kinematics and energetics with respect to the crack propagation-rate, as well as stiffness degradation of the material.

5.2.1 Crack propagation and strain energy release

In a continuum representation of the energetics of crack propagation using conventional linear elastic fracture mechanics, crack propagation takes place when the driving force measured in terms of the strain energy release-rate G exceeds a critical value G_C . For a mode I crack under plane stress conditions, G is related to the stress intensity factor (SIF) K_I by the expression (Anderson 2005):

$$GdA = -dU_{\text{strain}} + dW = \frac{K_I^2}{E_{\text{eff}}}dA \quad (28)$$

where dU_{strain} is the change in strain energy of the system, dW is the work done by external load, E_{eff} is the effective Young's modulus, dA is the incremental crack surface area and K_I is the stress intensity factor. The validity of the Eq. (28) is examined with results of the simulations by the concurrent atomistic–continuum model. The energy release increment measured by $-dU_{\text{strain}} + dW$ is calculated from parameters in the simulation and compared with the value of $\frac{K_I^2}{E_{\text{eff}}}dA$. For a square plate with a centered crack, K_I is estimated as $\sigma\sqrt{\pi a} \cdot \eta$, where σ is the far-field stress on the domain boundary and η is a geometric factor. The value of dA at a time t is approximated as $A(t) - A(t-dt)$, where dt is taken as 1 ps. The same difference approximation is made for all other variables in Eq. (28). The resulting strain energy release-rate characterized by the two terms is plotted as a function of the current crack length in Fig. 7. The two plots match very well through the crack propagation process, corroborating the validity of terms in Eq. (28) in the context of the concurrent model.

For crack propagation at low speeds, G should exceed a critical energy release-rate $G_C = 2\gamma_s$ to create a free surface, where γ_s is the surface energy per unit area. At high speeds, inertia effects comes into play that require higher energy release-rates to maintain the high crack propagation speed. Experimental studies e.g. in

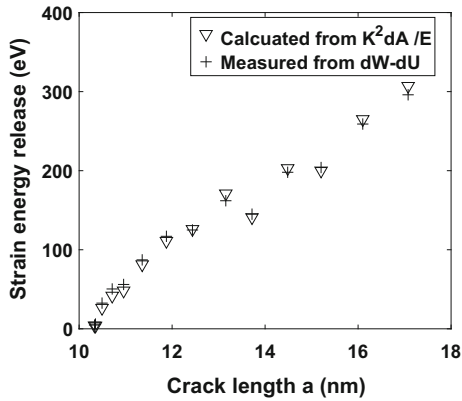
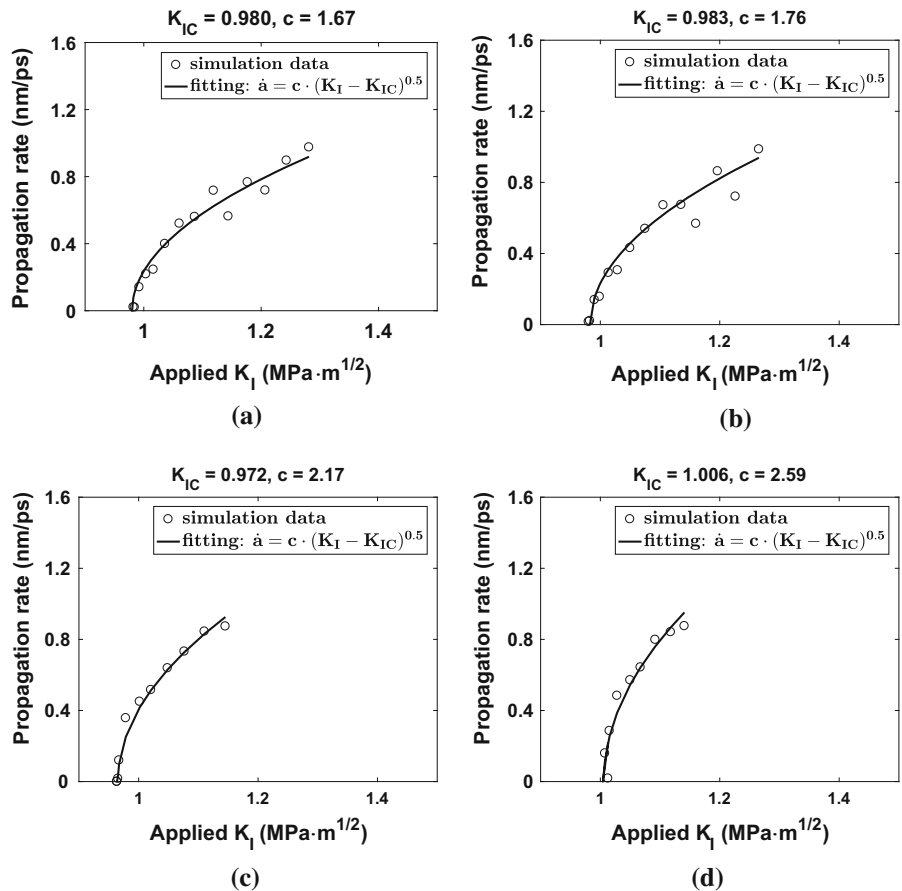


Fig. 7 Strain energy release-rate characterized by terms in Eq. (28) as a function of the crack length

Sharon and Fineberg (1999) have suggested G_C with dynamic effects to be:

$$G_C(v) = \frac{2\gamma_s}{(1 - \frac{v}{v_R})} \quad (29)$$

Fig. 8 Crack propagation-rate as function of the stress intensity factor K_I for different specimens, viz.: **a** $L = 100$ nm by concurrent model, **b** $L = 200$ nm by concurrent model, **c** $L = 100$ nm by MD and **d** $L = 50$ nm by MD



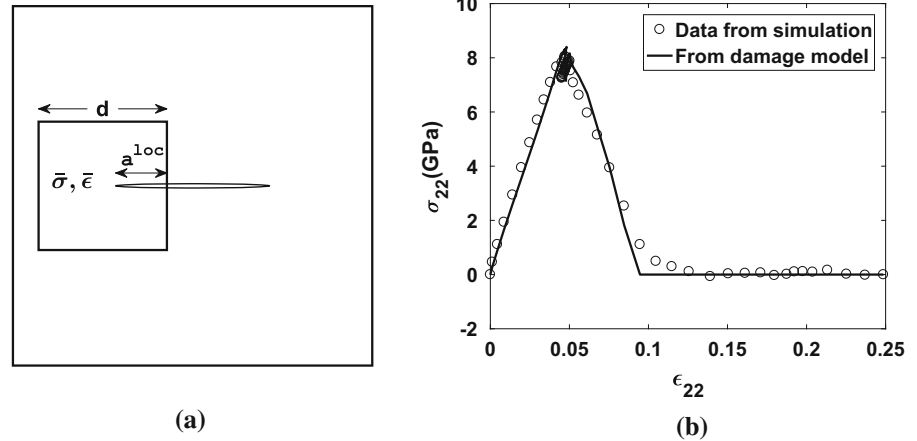
where v is the crack propagation velocity and v_R is the velocity of the Rayleigh wave. To investigate the correlation between applied loading and propagation speed, the crack propagation rate $v = da/dt$ using $dt = 1$ ps is plotted as a function of the stress intensity factor K_I in Fig. 8. The four plots correspond to specimen sizes $L = 100$ and 200 nm modeled by the concurrent model and specimen sizes $L = 50$ and 100 nm modeled by pure MD.

The results in Fig. 8 show that the crack propagation velocity does not increase linearly with the applied loading as a consequence of the inertia effect. The energy release-rate in Eq. (28) does exceed the critical value G_C given by Eq. (29). For a quantitative correlation, the following form is proposed to fit the data:

$$v = \dot{a} = \begin{cases} c \cdot (K_I - K_{IC})^{1/2}, & \text{if } K_I > K_{IC} \\ 0, & \text{otherwise} \end{cases} \quad (30)$$

where K_{IC} is the critical stress intensity factor with units of $\text{MPa} \cdot \sqrt{\text{m}}$ and c is a coefficient with the unit

Fig. 9 **a** The computational domain with an inspection window with a part of the growing crack and **b** comparison of the simulation stress with that evaluated from Eq. (31)



$\text{Pa}^{-0.5} \text{m}^{3/4} \text{s}^{-1}$. The parameters for the MD and the concurrent model with different specimen sizes are calibrated according to Eq. (29). The calibrated results are given in Fig. 8 for all four cases. For the sample size $L = 100 \text{ nm}$, both the concurrent and MD models give similar results. This concludes that the concurrent model developed has good accuracy with respect to the crack propagation process. Comparing the results of different specimen sizes $L = 50, 100$ and 200 nm , it is observed that results for $L = 100$ and 200 nm are quite similar. However K_{IC} and c values for $L = 50 \text{ nm}$ has a much larger deviation. This suggests that when $L \leq 100 \text{ nm}$ the boundary effects becomes important. To obtain correct parameters, sufficiently large domains that are afforded by the concurrent atomistic–continuum model are necessary.

5.2.2 Stiffness degradation with cracking

Crack evolution in the material domain causes a degradation of the overall stiffness. This degradation can be characterized using a simple scalar damage variable D introduced in conventional continuum damage mechanics (CDM) theories (Kachanov 1986). In these theories, the damage-induced degraded stiffness is related to the undamaged stiffness as:

$$\begin{aligned} c'_{ijkl} &= (1 - D)c_{ijkl} \quad \text{where} \\ \sigma'_{ij} &= c'_{ijkl}\epsilon_{ij} \quad \text{and } D \in [0, 1] \end{aligned} \quad (31)$$

where c'_{ijkl} and c_{ijkl} are the damaged and undamaged stiffnesses, and σ'_{ij} is the stress in the damaged medium. Consider a square inspection window of dimension d

in the computational domain, as shown in Fig. 9a. It contains a part of the crack of local length a^{loc} extending through the z -direction. The square window has a dimension $d = 5 \text{ nm}$ and its center is located 5 nm in front of the initial position of the crack tip. Following Kachanov (1986), the scalar damage variable D may be related to the crack length a^{loc} by the relation $D = \frac{a^{\text{loc}}}{d}$. To verify if the damage relations are justified for the concurrent model, the simulated volume-averaged stress $\bar{\sigma}_{ij}$ in the inspection window is compared with the stress $\bar{\sigma}'_{ij}$ calculated from Eq. (31) using the calibrated stiffness components c_{ijkl} in Table 1 and volume-averaged strain $\bar{\epsilon}_{ij}$ for the window. The stresses are compared in Fig. 9b and are seen to have a good match throughout the strain history from no damage to complete damage. In summary, a set of relations describing brittle crack propagation for single crystal nickel (100) surface is derived from the concurrent model simulations and expressed as a combination of Eqs. (28), (30) and (31).

5.3 Strain-rate and temperature effects on the critical stress for crack propagation

Investigation of strain-rate and temperature effects on crack propagation is motivated by two reasons. The first is to validate that the finite temperature coupled model maintains the proper statistical mechanics property of the system. The second reason is to obtain a better understanding of crack propagation under experimental strain-rate conditions, which cannot be directly achieved by MD or the coupled atomistic–continuum model. For pure MD simulations, the choice

Fig. 10 **a** Temperature dependence of the critical stress for a fixed applied strain-rate and **b** the strain-rate dependence of the critical stress for a fixed temperature

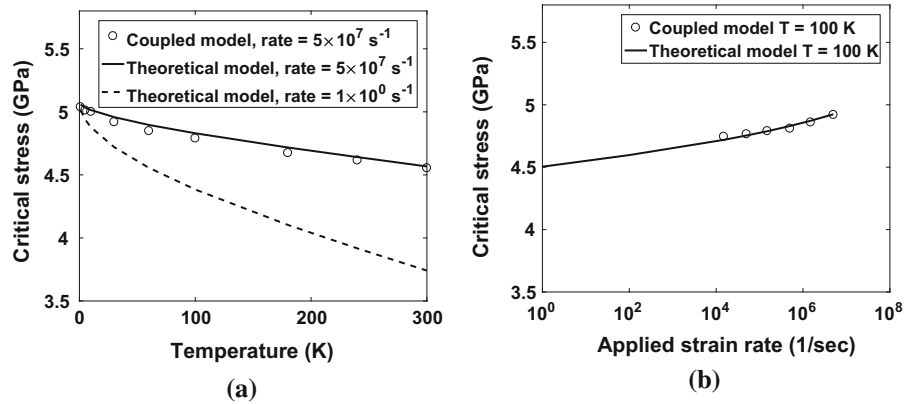


Table 2 Parameters used in Eq. (32)

T_m	E	$N \nu_0$	$Q_0(\sigma)$	A	σ_C	α
1728 K	164 GPa	$4 \times 10^{12} \text{s}^{-1}$	$A(1 - \sigma/\sigma_C)^\alpha$	9.05 eV	5.12 GPa	1.9

of extremely small time-steps (order of femto-seconds) results in very high strain-rates. This can jeopardize the analysis of thermally activated processes. The coupled concurrent model reduces the degrees of freedom significantly compared with full MD model. This enables carrying out simulations at 1–2 orders of magnitude lower strain-rates for the same computational cost of the MD model. With this advantage, the coupled concurrent model is used effectively to study the temperature and strain-rate effects on the critical stress for crack propagation. The results are compared with predictions by a theoretical model in [Zhu et al. \(2008\)](#).

For a thermally activated process under constant strain rate $\dot{\epsilon}$ and temperature T , the most probable nucleation stress satisfies following condition:

$$\frac{Q(\sigma, T)}{k_B T} = \ln\left(\frac{k_B T N \nu_0}{E \dot{\epsilon} \Omega(\sigma, T)}\right) \quad (32)$$

where $Q(\sigma, T)$ is the stress and temperature dependent activation free energy, k_B is the Boltzman constant, N is number of nucleation sites, ν_0 is the attempt frequency, E is the stiffness and Ω is the activation volume given as $\Omega(\sigma, T) = -\frac{\partial Q(\sigma, T)}{\partial \sigma}$. It is suggested in [Zhu et al. \(2008\)](#) that the temperature dependence can be expressed as $Q(\sigma, T) = (1 - T/T_m)Q_0(\sigma)$, where T_m is the melting temperature and $Q_0(\sigma)$ represents the energy barrier as function of the applied stress.

The temperature dependence and strain-rate dependence of the critical stress for crack propagation, using

the coupled concurrent model with finite temperature, is shown in [Fig. 10](#). The simulated results are compared with predictions from the theoretical model in [Eq. \(32\)](#), using parameters given in [Table 2](#). The good match between the results confirms that the coupled model is able to capture the statistical mechanics property of the system at various temperatures and strain-rates in the atomistic domain. Furthermore through parameter fitting, the critical stress at realistic strain-rates can be estimated. Given the relation between stress and the stress intensity factor, the result demonstrates how the temperature and applied strain-rate affect K_C in crack propagation law of [Eq. \(30\)](#). Such effect on the coefficient c however remains unclear at this time.

6 Accuracy and efficiency of simulations with the self-consistent constitutive-crack evolution model

The self-consistent crack propagation model, obtained from the concurrent coupled atomistic–continuum model, is implemented in a continuum finite element model. For verification of the self-consistent model, results from the two models are compared. Three major considerations are needed for the continuum FE model, viz. (i) the nonlinear and nonlocal elasticity relations introduced in [Sect. 4](#), (ii) the crack propagation model described by [Eq. \(30\)](#), and (iii) the crack represen-

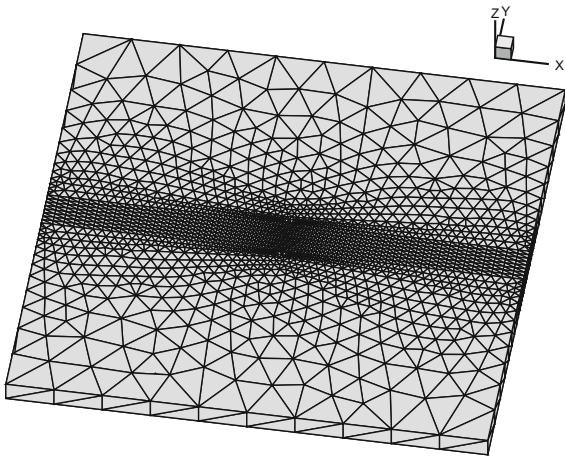


Fig. 11 The FE mesh in the continuum model implemented with crack propagation law

tation and stiffness degradation due to the crack in Eq. (31). The parameters in Eq. (30) are derived from simulations with the concurrent model for the specimen with $L = 100$ nm. They are calibrated as of $K_{IC} = 0.980 \text{ MPa}\cdot\sqrt{\text{m}}$ and $c = 1.67 \text{ Pa}^{-0.5}\cdot\text{m}^{3/4}\text{s}^{-1}$. For numerical stability, the maximum damage parameter D_{max} in Eq. (31) is set to be 0.9995.

The continuum finite element domain has the same geometry as the concurrent model with dimensions $200 \text{ nm} \times 200 \text{ nm} \times 4.224 \text{ nm}$, shown in Fig. 3a. The domain is discretized into approximately 20,000 4-noded CST tetrahedral elements depicted in Fig. 11. An initial centered crack of length $a_0 = 10$ nm introduced in the FE domain by changing the initial value of the damage variable to $D = 0.9995$ in highly refined elements that represent the crack. The domain is subjected to the same biaxial displacement loading considered in Sect. 5. While CST elements are known to exhibit mesh dependency near the crack tip for local models, the *non-local model* in this study, along with the substantially refined mesh are sufficient to mitigate mesh dependency.

The results of simulations by the pure FE model and the concurrent atomistic–continuum model are presented in Fig. 12. Figure 12a compares the crack-tip stress distribution at the beginning of the propagation process. The energy release-rate is plotted as a function of the increasing crack length in Fig. 12b, and the crack propagation-rate as a function of the applied stress intensity factor is depicted in Fig. 12c. Generally good concurrence of results by the two models is seen

for all three plots. This results provide confidence in the effectiveness of the crack related constitutive and damage models for single crystal Ni, in Eqs. (22), (30) and (31) obtained from the multi-scale model.

The computational efficiency of the concurrent multi-scale model, as well as the self-consistent model based pure FE model, are compared in Table 3. The computational cost is made in terms of the cumulative CPU hours incurred for simulations by the full MD model, the concurrent model and the full FE model with the self-consistent constitutive and crack propagation relations. Simulations are conducted on a specimen of dimensions $L_x = L_y = 200$ nm, $L_z = 4.224$ nm. The boundary conditions are as discussed before, with the applied biaxial strain reaching the values $\epsilon_{11} = \epsilon_{22} = 3.5\%$, $\sigma_{33} = 0$. The results in Table 3 show a reduction in total CPU hours by a factor of 7 from MD to the concurrent model. An additional reduction by a factor of 71 is achieved when transitioning from the concurrent to the full FE model. This corresponds to a net speed-up by a factor of 500 from full MD to full FE simulation simulations. This tremendous computational efficiency provides the capability of efficiently simulating microscale experiments, while accurately tracking material behavior origins at the atomistic length-scale.

7 Summary and discussions

A multi-scale computational framework, coupling atomistic and continuum models of elastic crystalline materials, is developed in this paper with the goal of formulating self-consistent constitutive and crack evolution models for use in finite element analyses. The concurrent, coupled atomistic–continuum model is able to attain atomic level interactions and deformation mechanisms especially near crack tips, while affording continuum scale physical loading conditions. Atomistic modeling is done using molecular dynamics (MD) using the LAMMPS, while the continuum modeling for quasi-static loading is done using a crystal elasticity finite element analysis code. Finite temperature conditions are applied to the atomistic domain using Langevin dynamics for the MD model. The atomistic–continuum coupling is achieved by enforcing geometric compatibility and force equilibrium in a finite-thickness handshake interphase region. An efficient staggered solution algorithm together with a sub-stepping method is used to solve for the equilibrium

Fig. 12 Comparing results of simulations by the pure FE model and the concurrent atomistic–continuum model: **a** stress distribution near the crack tip, **b** strain energy release-rate as a function of the increasing crack length, **c** crack propagation-rate as a function of the applied stress intensity factor

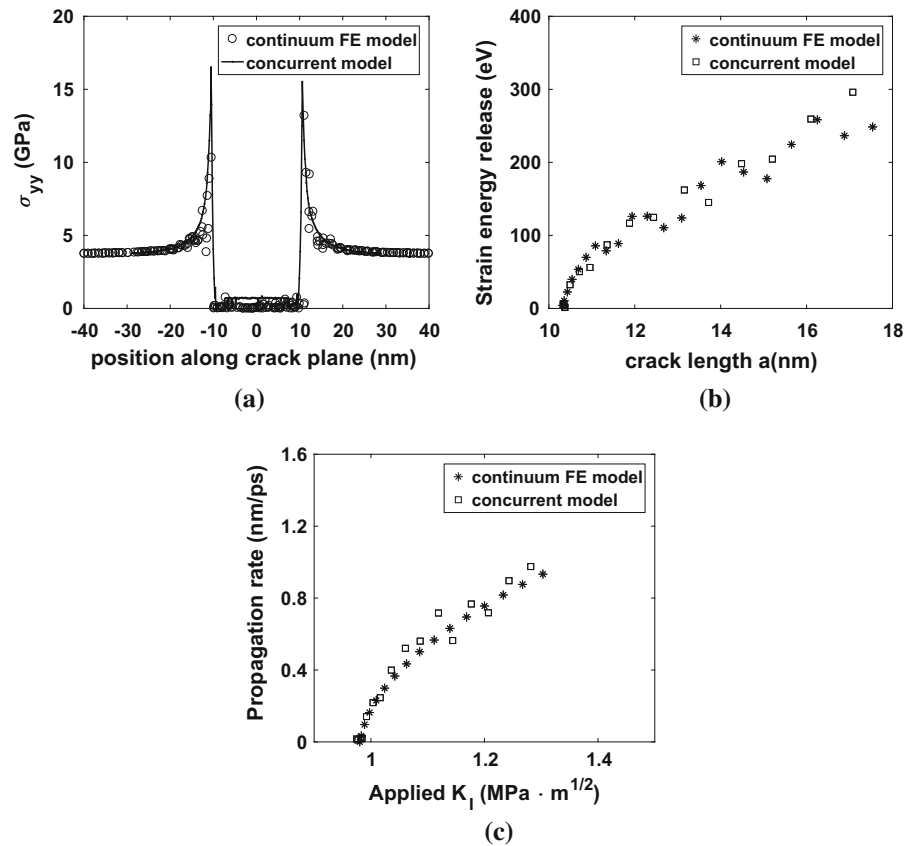


Table 3 Comparison of computational cost by different models in CPU hours, expressed as the number of CPUs multiplied by hours per CPU

Method	MD	Concurrent atomistic–continuum	FE
DoF	1.6×10^7 atoms	1.6×10^6 atoms + 2×10^4 elements	2×10^4 elements
Computational cost	3500	500	7

configuration of the coupled model. A high performance parallel implementation is invoked for the coupled LAMMPS and FE codes.

For a material with a static crack, the self-consistent constitutive model for a single crystal nickel with EAM potential takes the form of a nonlinear and nonlocal crystal elasticity relation. In the next stage, the concurrent model simulates crack propagation with the crack contained in the MD domain. For single crystal nickel under mode I loading, it is observed that crack propagates by bond cleavage with accelerated speed until dislocations start to nucleate. For the brittle crack propagation regime, the crack propagation-rate, energy release rate and stress distributions are investi-

gated. These simulations provide augmentation of the self-consistent model for crack propagation through a quantitative relation between the strain energy release rate, the stress intensity factor and effective modulus. Furthermore, stiffness degradation is characterized by a damage model, where the damage parameter is related to the crack length. Validation studies of the concurrent model with MD simulations show excellent concurrence with respect to crack propagation rate and history, as well as the stress distribution. Size dependence study shows convergence with larger specimen size due to mitigated boundary effects.

Finally, the effectiveness of the derived self-consistent constitutive and crack propagation relations is tested

through simulations by continuum-scale finite element model implementing the self-consistent model. The results show excellent match in the crack propagation history, energy release rate and stress distributions by the full FE and concurrent models. A significant reduction in the degrees of freedom and increase in computational efficiency can be attained by transitioning from a full MD to a FE model. This tremendous computational efficiency provides the capability of efficiently simulating microscale experiments, while accurately tracking material behavior origins at the atomistic length-scale. Extension of this coupled model to formulate constitutive models for plasticity is currently under way and will be reported in future publications.

Acknowledgements This work has been supported by a mechanics of materials and strength, materials and surface engineering research program sponsored by the National Science Foundation, Mechanics and Structure of Materials Program through Grant No. CMMI-1200231 (Program Manager: Dr. Alexis Lewis). The authors gratefully acknowledge this support. Computing support by the Homewood High Performance Compute Cluster (HHPC) and Maryland Advanced Research Computing Center (MARCC) is gratefully acknowledged. Finally authors thank Subhendu Chakraborty, Jiahao Cheng, Shu Guo for important discussions.

References

- Abraham F, Brodbeck D, Rudge W, Xu X (1997) A molecular dynamics investigation of rapid fracture mechanics. *J Mech Phys Solids* 45:1595–1619
- Aifantis EC (1984) On the microstructural origin of certain inelastic models. *J Eng Mater Technol* 106(4):326–330
- Anderson TL (2005) *Fracture mechanics: fundamentals and applications*. CRC Press, Boca Raton
- Askes H, Aifantis EC (2011) Gradient elasticity in statics and dynamics: an overview of formulations, length scale identification procedures, finite element implementations and new results. *Int J Solids Struct* 48:1962–1990
- Badia S, Bochev P, Lehoucq R, Parks M, Fish J, Nugehally MA, Gunzburger M (2007) A force-based blending model for atomistic-to-continuum coupling. *Int J Multiscale Comput Eng* 5(5):387–406
- Badia S, Parks M, Bochev P, Gunzburger M, Lehoucq R (2008) On atomistic-to-continuum coupling by blending. *Multiscale Model Simul* 7(1):381–406
- Budiansky B (1965) On the elastic moduli of some heterogeneous materials. *J Mech Phys Solids* 13:223–227
- Columbus D, Grujicic M (2001) A comparative discrete-dislocation/nonlocal crystal-plasticity analysis of plane-strain mode I fracture. *Mater Sci Eng A* 180:138–161
- Farrissey L, Ludwig M, McHugh PE, Schmauder S (2000) An atomistic study of void growth in single crystalline copper. *Comput Mater Sci* 18(1):102–117
- Ghosh S (2011) *Micromechanical analysis and multi-scale modeling using the Voronoi cell finite element method*. CRC Press, Boca Raton
- Grujicic M, Cao G, Batchu S (2003) Crystal plasticity-based finite element analysis of deformation and fracture of polycrystalline lamellar γ -tial + α 2-ti₃al alloys. *J Mater Sci* 38:209–232
- Gumbsch P (1995) An atomistic study of brittle fracture: toward explicit failure criteria from atomistic modeling. *J Mater Res* 10:2897–2907
- Hill R (1965) A self-consistent mechanics of composite materials. *J Mech Phys Solids* 13:213–222
- Honeycutt D, Anderson H (1987) Molecular dynamics study of melting and freezing of small Lennard-Jones clusters. *J Chem Phys* 91:4950–4963
- Kachanov LM (1986) *Introduction to continuum damage mechanics*. Springer, Berlin
- Kadav K, Germann T, Lomdahl P (2006) Molecular dynamics comes of age: 320-billion-atom simulation on BlueGene/L. *Int J Mod Phys* 17:1755–1761
- Maranganti R, Sharma P (2007) A novel atomistic approach to determine strain-gradient elasticity constants: tabulation and comparison for various metals, semiconductors, silica, polymers and the (ir) relevance for nanotechnologies. *J Mech Phys Solids* 55(9):1823–1852
- Miller R, Ortiz M, Phillips R, Shenoy V, Tadmor E (1998) Quasicontinuum models of fracture and plasticity. *Eng Fract Mech* 61(3):427–444
- Mishin Y, Farkas D, Mehl M, Papaconstantopoulos D (1999) Interatomic potentials for monoatomic metals from experimental data and ab initio calculations. *Phys Rev B* 59(5):3393
- Ortiz M, Pandolfi A (1999) Temperature and strain-rate dependence of surface dislocation nucleation. *Int J Numer Methods Eng* 44:1267–1282
- Plimpton S (1995) Fast parallel algorithms for short-range molecular dynamics. *J Comput Phys* 117:1–19
- Roe KL, Siegmund T (2003) An irreversible cohesive zone model for interface fatigue crack simulation. *Int J Numer Method Eng* 70:307–322
- Saether E, Yamakov V, Glaesgen EH (2009) An embedded statistical method for coupling molecular dynamics and finite element analyses. *Int J Numer Methods Eng* 78(11):1292–1319
- Sarma V, Reddy P (1973) Third-order elastic constants of single crystal nickel at 800 K. *Phys Status Solid (a)* 16(2):413–418
- Sharon E, Fineberg J (1999) Confirming the continuum theory of dynamic brittle fracture for fast cracks. *Nature* 397(6717):333–335
- Shenoy V, Miller R, Tadmor E, Rodney D, Phillips R, Ortiz M (1999) An adaptive finite element approach to atomic-scale mechanics—the quasicontinuum method. *J Mech Phys Solids* 47(3):611–642
- Shimomura Y, Kiritani M, Mukouda I (2003) Computer simulation study of the atomistic mechanism of deformation and fracture initiation in thin FCC metal films. *Mater Sci Eng A* 350(1–2):238–244
- Spearot D, Jacob K, McDowell D (2004) Non-local separation constitutive laws for interfaces and their relation to nanoscale simulations. *Mech Mater* 36:825–847

- Tadmor EB (1996) The quasicontinuum method. Ph.D. thesis, Brown University
- Xiao S, Belytschko T (2004) A bridging domain method for coupling continua with molecular dynamics. *Comput Methods Appl Mech Eng* 193(17):1645–1669
- Xiong L, Deng Q, Tucker GJ, McDowell DL, Chen Y (2012) Coarse-grained atomistic simulations of dislocations in Al, Ni and Cu crystals. *Int J Plast* 38:86–101
- Yamakov V, Saether E, Phillips DR, Glaessgen EH (2006) Molecular-dynamics simulation-based cohesive zone representation of intergranular fracture processes in aluminum. *J Mech Phys Solids* 54(9):1899–1928
- Yamakov V, Saether E, Glaessgen E (2008) Multiscale modeling of intergranular fracture in aluminum: constitutive relation for interface debonding. *J Mater Sci* 43:7488–7494
- Zhang J, Ghosh S (2013) Molecular dynamics based study and characterization of deformation mechanisms near a crack in a crystalline material. *J Mech Phys Solids* 61(8):1670–1690
- Zhou S, Lomdahl P, Voter A, Holian B (1998) A molecular dynamics investigation of rapid fracture mechanics. *Eng Fract Mech* 61:173–187
- Zhou X, Zimmerman J, Reedy E, Moody N (2008) Molecular dynamics simulation based cohesive surface representation of mixed mode fracture. *Mech Mater* 40:832–845
- Zhu T, Li J, Yip S (2004) Atomistic study of dislocation loop emission from a crack tip. *Phys Rev Lett* 93(2):025503
- Zhu T, Li J, Samanta A, Leach A, Gall K (2008) Temperature and strain-rate dependence of surface dislocation nucleation. *Phys Rev Lett* 100(2):025502
- Zimmerman JA, Bammann DJ, Gao H (2009) Deformation gradients for continuum mechanical analysis of atomistic simulations. *Int J Solids Struct* 46(2):238–253